Mon. Not. R. Astron. Soc. **373,** 1091–1106 (2006) doi:10.1111/j.1365-2966.2006.11089.x

Supersonic turbulence, filamentary accretion and the rapid assembly of massive stars and discs

Robi Banerjee,[1,2]★ Ralph E. Pudritz[2,3] and Dave W. Anderson[2]

[1]*Institute of Theoretical Astrophysics (ITA), University of Heidelberg, Germany*
[2]*Department of Physics and Astronomy, McMaster University, Hamilton, Ontario L8S 4M1, Canada*
[3]*Origins Institute, McMaster University, Arthur Bourns Bldg 241, Hamilton, Ontario L8S 4M1, Canada*

Accepted 2006 September 20. Received 2006 September 15; in original form 2006 August 2

ABSTRACT

We present a detailed computational study of the assembly of protostellar discs and massive stars in molecular clouds with supersonic turbulence. We follow the evolution of large-scale filamentary structures in a cluster-forming clump down to protostellar length-scales by means of very highly resolved, 3D adaptive mesh refined (AMR) simulations, and show how accretion discs and massive stars form in such environments. We find that an initially elongated cloud core which has a slight spin from oblique shocks collapses first to a filament and later develops a turbulent disc close to the centre of the filament. The continued large-scale flow that shocks with the filament maintains the high density and pressure within it. Material within the cooling filament undergoes gravitational collapse and an outside-in assembly of a massive protostar. Our simulations show that very high mass accretion rates of up to 10^{-2} $M_{\odot}$ yr^{-1} and high, supersonic, infall velocities result from such filamentary accretion. Accretion at these rates is higher by an order of magnitude than those found in semi-analytic studies, and can quench the radiation field of a growing massive young star. Our simulations include a comprehensive set of the important chemical and radiative processes such as cooling by molecular line emission, gas–dust interaction and radiative diffusion in the optically thick regime, as well as H_2 formation and dissociation. Therefore, we are able to probe, for the first time, the relevant physical phenomena on all scales from those characterizing the clump down to protostellar core.

Key words: turbulence – methods: numerical – ISM: clouds – ISM: evolution.

1 INTRODUCTION

Arguably, the most comprehensive theoretical picture that we have of star formation is that stars are a natural consequence of supersonic turbulence within self-gravitating, molecular clouds (see recent reviews Elmegreen & Scalo 2004; Mac Low & Klessen 2004; Ballesteros-Paredes et al. 2006). It has been appreciated for some time that turbulence could play an important role in controlling the formation of cosmic structure in general and stars in particular (e.g. von Weizsäcker 1951). Supersonic turbulence is observed in most if not all giant molecular clouds (GMCs) and is important because it rapidly sweeps up large volumes of gas and compresses it into systems of dense filaments. The density jump that is associated with isothermal shock waves of Mach number $\mathcal{M}$ scales as $\simeq\mathcal{M}^2$, so that this process may ultimately be responsible for forming the dense clumps and cores seen in molecular clouds (e.g. Padoan 1995). An attractive aspect of this theory is that since turbulence is associated with a broad spectrum of velocities, a large range of physical scales and masses should arise for both the filamentary structure, as well as the properties of the dense clumps and cores that form within them.

Observational surveys confirm that filamentary substructure characterizes the internal organization of molecular clouds on many scales. It is clearly evident in the Orion A molecular cloud (e.g. Johnstone & Bally 1999) where, in addition to showing the obvious integral-filament shaped structure, one also sees smaller structures of 1.3 pc in scale. James Clerk Maxwell Telescope submillimetre studies of Orion B (Mitchell et al. 2001) reveal a plethora of filamentary structures and their embedded cores. This pattern is also seen in the observational studies by Fiege et al. (2004), wherein a few bright cores are seen to be embedded in a larger, isolated filamentary structure. Similar results are also seen in more embedded regions such as the Lupus 3 cloud, where strong links between filaments and emerging star clusters are observed (Teixeira, Lada & Alves 2005).

Computational studies of turbulence (e.g. Porter, Pouquet & Woodward 1994) have made important progress over the last decade both in their dynamic range and in the list of physical processes that have been added to them. Simulations show that the shocks that

★E-mail: banerjee@ita.uni-heidelberg.de

are created in supersonic turbulence produce a rich filamentary substructure. A broad spectrum of smaller, condensed regions is also produced (e.g. Klessen & Burkert 2000; Padoan & Nordlund 2002). Detailed comparisons with the observations show that there is a good correspondence between numerically determined core mass spectra and the submillimetre surveys of star-forming cores in molecular clouds (e.g. Tilley & Pudritz 2004) (henceforth TP04). One of the most important consequences is that the core mass spectrum (CMS) is found to be similar to that of the initial mass function (IMF) that characterizes the stellar mass spectrum. Cores in these numerical experiments are also born with a broad distribution of spins, which are a consequence of the oblique shocks that create them (e.g. TP04). The general velocity field created in simulations of compressible gas has also been shown to have a very good correspondence with that observed molecular cloud spectra (Falgarone et al. 1994). Finally, structure formation in supersonic flows occurs rapidly – typically in a sound crossing time or two. This can in principle account for the rapid time-scales that characterize the formation of star clusters such as the Orion Nebula Cluster (ONC) – whose members have a mean age <1 Myr with a spread of less than 2 Myr (Hillenbrand 1997). Thus, the universal properties of turbulence potentially provide a comprehensive explanation for the broad range in stellar masses and spins that characterize star formation wherever we have been able to measure it.

The turbulent fragmentation theory of star formation makes a much broader range of testable predictions than the older theory that featured the gravitational collapse of nearly spherical, isolated cores, often characterized as singular isothermal spheres. This latter picture did not provide a clear physical explanation for the origin of the IMF. Moreover, the model predicted that accretion rates that are related to the cube of the (isothermal) sound speed c, i.e. $\dot{M}_a \simeq c^3/G$. While adequate to explain the formation of low-mass stars in atypical clouds, such as Taurus, this accretion rate is orders of magnitude too small to account for the formation of high-mass stars in observed regions of clustered star formation, such as the Orion Nebula (see Beuther et al. 2006, for recent review). It is known that accretion rates of the order of $10^{-3}\,\mathrm{M}_\odot\,\mathrm{yr}^{-1}$ can overcome the effects of radiation pressure and result in massive star formation (Wolfire & Cassinelli 1987). It has been suggested that the cores in which massive stars form can achieve these high rates essentially due to the high turbulent pressure that is found in such regions (e.g. McLaughlin & Pudritz 1997; McKee & Tan 2003).

While high pressure must play an important role in the formation of massive stars, these latter theoretical studies did not address how it is that low-mass stars would form in the high-pressure region that is producing the massive stars – both populations are co-spatial. Moreover, it has been shown in simulations that the turbulence envisaged to drive a high mass accretion rate on to a single massive star will instead fragment the gas into smaller pieces quite rapidly (Dobbs, Bonnell & Clark 2005). Turbulence creates structure, and it is this structure, not pressure, that ultimately determines mass flow.

A more fundamental shortcoming of the isolated core picture is that it fails to explain how stars can span more than three decades in mass. While the process of ambipolar diffusion – often invoked in older models as a regulator of gravitational collapse of isolated magnetized cores (e.g. Shu, Adams & Lizano 1987) – certainly does mediate the eventual collapse of sufficiently massive cores, it does not provide a first-principles explanation for why such a wide range of stellar masses should exist in the first place. Similarly, Jeans mass arguments to 'predict' stellar masses are not really very predictive when applied to media that are dominated by large density contrasts. As low- and high-mass stars form in clusters and are essentially co-spatial, they are likely to acquire their masses by similar mechanisms. In both cases, we expect that filamentary accretion will play a role in the accumulation of the cores out of which they form.

In this paper, we explore the multiscale nature of the formation of filamentary large-scale structure and how this controls the formation of protostellar discs and stars in turbulent cluster-forming clumps (these have typical sizes of <1 pc). We accomplish this by using an adaptive mesh refinement (AMR) code known as FLASH (Fryxell et al. 2000). Our 3D hydrodynamical AMR simulations include many physical processes such as cooling due to dust, molecules, molecular hydrogen dissociation, as well as radiative diffusion out of optically thick regions. We use as initial conditions numerical data from our recent simulations of cluster formation in molecular clumps (TP04) that show that a complete mass spectrum of gravitationally bound cores can be formed by supersonic turbulence within molecular clouds that closely resemble the core mass function of clouds such as Orion.

We follow the filament that forms the first massive star in our simulation, and find that it has high density and dynamic pressure that is maintained by continued inflow and shocking into the filaments. The collapse of this dense material along the filament and into the disc and star is the key to understanding this problem. Lower mass stars in this picture also form in filamented structure, but which are less compressed and on smaller scales. Our simulations trace how the most massive star-forming region is assembled and how collapse and the formation of protostellar discs can occur, by resolving the local Jeans length down to scales approaching that of the protostar itself.

We find that filaments play a dominant role in controlling the physics, accretion rate and angular momentum of the much smaller scale accretion disc that forms within such collapsing structures (see also Balsara, Ward-Thompson & Crutcher 2001). Large-scale filamentary flows sustain accretion rates that are orders of magnitude greater than both (i) the naive scalings that are derived from the virial theorem applied to uniform, 3D media or even (ii) the collapse of isolated Bonner–Ebert spheres. The large-scale structuring of molecular clouds into filaments therefore has profound effects on the rate of formation of discs and stars.

The formation and subsequent fragmentation of large-scale filaments can also lead to the formation of (massive) binaries or multiple star systems which was shown in a series of smoothed particle hydrodynamics simulations (e.g. Turner et al. 1995; Whitworth et al. 1995; Bhattal et al. 1998). In those studies, fragmentation is mainly the result of the complete formation of molecular hydrogen (which reduces the temperature in the cloud cores at high densities) during the gravitational collapse of the large-scale filament.

This paper proceeds by first describing our initial conditions and numerical procedures (Section 2). We then go on to systematically study the evolution of large-scale filaments (Section 3) that feed the formation of a massive star, the formation and evolution of an accretion disc (Section 4), and finally the accretion of the central star (Section 5) within the disc. We conclude our results in the discussion in Section 6 and give a compilation of our cooling approach in Appendix A.

2 NUMERICAL METHOD AND INITIAL CONDITIONS

Many studies of star formation have examined the self-similar collapse of highly idealized structures such as singular isothermal spheres. An initial state that is much closer to observational reality is the 3D Bonner–Ebert sphere – whose collapse has received

far less theoretical attention until recently. In Banerjee, Pudritz & Holmes (2004) and Banerjee & Pudritz (2006), we adapted the FLASH code for star formation applications and studied the three-dimensional collapse of rotating, magnetized and non-magnetized, Bonnor–Ebert spheres (Ebert 1955; Bonnor 1956). We will compare our simulations with the results of the collapse of isolate BE models later in the paper. As noted above, however, isolated objects like this are not typical structures of observed molecular clouds.

This paper attacks the broader problem of the physical connection between large-scale structure formation (in this instance, on the scale of the cluster-forming clump) and star formation. We use as initial conditions the final state of simulations of turbulent core formation presented by TP04. The goal of this latter study was to study the origin of the core mass function in cluster-forming clumps, and to identify the physical conditions that best matched the observations. As documented below, we found that there was a particular set of conditions that produced realistic properties of molecular cloud cores and that also abounded in filamentary-like structures.

The TP04 simulations were hydrodynamic and were performed with the ZEUS 3D code (Stone & Norman 1992a,b) on a static grid and had to be stopped at the point when the density of any of formed cloud cores reached the critical density of the Truelove criterion (Truelove et al. 1997). Using the FLASH code (Fryxell et al. 2000) which is based on the PARAMESH AMR technique (Olson et al. 1999) allows us to follow the collapse of the TP04 cores over many orders of magnitude in density and length-scale without under-resolving the relevant physical scales.

In practice, we took the raw simulation data (velocity and density) from one of the later output files in TP04, which are available in Hierarchical Data Format (HDF) format, and initialized the FLASH variables with these ZEUS data. During the initialization, we use a Jeans refinement criterion where we resolve the local Jeans length,

$$\lambda_{\rm J} = \left(\frac{\pi c^2}{G\,\rho}\right)^{1/2}, \qquad (1)$$

by at least eight grid points (c is the isothermal sound speed, ρ is the matter density and G is the Newton's constant). This density-dependent initialization results in an initially non-homogeneous grid structure compared to the homogeneous ZEUS 3D grid. By de-resolving the low-density regions in the simulations box, we can save a substantial amount of computational time without under-resolving the physical scales which are governed by the Jeans length during the collapsing stage. In Fig. 1, we show a 2D slice of the initial grid structure as 'seen' by the FLASH code.

For the subsequent simulation, we increased the resolution of the Jeans length to at least 12 grid points. Note that the Truelove criterion recommends that the Jeans length is resolved by only four grid points to avoid numerical fragmentation and ensure convergence.

2.1 Initial physical parameters

For the initial setup, we take the late-stage numerical data of run B5 from the TP04 simulations. This run has the following initial values for the side length of the simulation box $L = 9.8 \times 10^{17}$ cm $= 0.32$ pc, total mass $M_{\rm tot} = 105.1\,{\rm M}_\odot$, isothermal sound speed $c = 0.408\,{\rm km\,s^{-1}}$ and a rms velocity $v_{\rm rms} = 5\,c$ with a Kolmogorov-type spectrum, respectively. The simulation run B5 resulted in a mass spectrum of bound cores that has a Salpeter slope at high masses (in agreement with the observations). At the very highest masses, one finds a few objects, the most massive of which was the first to collapse. This is the object whose collapse we continued to follow with the FLASH code.[1] At the time we restarted the collapse simulation with the FLASH code, the peak mass density is $1.35 \times 10^{-15}\,{\rm g\,cm^{-3}}$ which corresponds to an initial free-fall time, $t_{\rm ff} = \sqrt{3\pi/32G\rho} \approx 1800$ yr. The mass enclosed within a radius of 2×10^{17} cm around the peak density, which is approximately the size of the cloud core, is $\sim 23\,{\rm M}_\odot$. This is also the Jeans mass of the initial TP04 simulation and represents a fairly massive cloud core mass and its evolution can be compared to the collapse simulation presented in Banerjee et al. (2004) and Banerjee & Pudritz (2006) which are based on the physical properties of a $170\,{\rm M}_\odot$ cloud core and the $2.1\,{\rm M}_\odot$ cloud core Barnard 68 observed by Alves, Lada & Lada (2001).

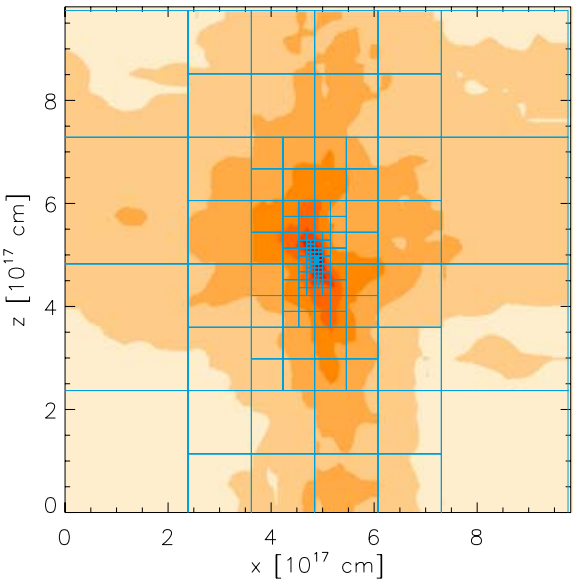

Figure 1. Initial setup as 'seen' by the FLASH code. The low-density (density shown in grey-scale) areas are less refined due to the applied Jeans refinement criterion. The resolution is indicated by the square blocks where each 3D block has 8^3 grid points.

2.2 Cooling

We extended the physical and chemical parameter space used in our earlier work to incorporate the relevant cooling processes important for star formation in molecular clouds. These processes are summarized in complete detail in Appendix A to which we refer the reader for further information. We included cooling by molecular line emission, cooling from gas–dust interactions, radiative diffusion in the optically thick regime and cooling by H_2 dissociation.

For the remainder of this subsection, we give the more general reader an idea of how we proceeded (one may wish to go directly to the results in Section 3). We first draw a distinction between the optically thin and optically thick regimes. For molecular line emission in the optically thin limit, we used the cooling rates due to Neufeld, Lepp & Melnick (1995), as employed in Banerjee et al. (2004) and

[1] For better visualization, we shifted the all simulation variables so that the peak density appears at the simulation centre before we rerun the FLASH simulation. This could be done without changing any physical properties as both simulations use periodic boundary conditions.

Banerjee & Pudritz (2006). Cooling by gas–dust transfer in the optically thin regime was treated as in Goldsmith (2001). We show in Appendix A that the dust temperature approaches the gas temperature at densities exceeding $n > 10^{7-9}$ under typical conditions. Even under these conditions, however, we find that the dust is still a very efficient coolant.

In the optically thick regime, the radiation from the dust surfaces (equation A4) cannot escape instantaneously and, by definition, the mean free path of the radiation field ($\sim 1/\kappa$) becomes smaller than the typical core size of the dense core. For most collapse situations, the core size is given by the core's Jeans length, $\lambda_{\rm J} = \sqrt{\pi c_{\rm s}^2 / G_N \rho_{\rm core}}$. Therefore, we estimate the optical depth as

$$\tau \approx \kappa \, \lambda_{\rm J}, \tag{2}$$

where κ is the dust opacity. This approximation is in accordance with the results from opacity-limited fragmentation and star formation by Low & Lynden-Bell (1976) and Silk (1977) who use the expression above in their studies.

Using the fact that the dust temperature gets close to the gas temperature (see the above section), we can use equations (A5) and (2) to estimate the critical density at which the gas is not cooled efficiently, i.e. when $\tau = 1$,

$$n_{\rm crit} = 2.1 \times 10^{10} \left(\frac{T}{20\,{\rm K}} \right)^{-5} \ {\rm cm}^{-3}. \tag{3}$$

In Banerjee et al. (2004), we showed that this critical density can be used to estimate the distance from the centre at which the first shock fronts build up. By updating our previous results with the above critical density, we find

$$r_{\rm crit} \sim 17 \ {\rm au} \left(\frac{n_{\rm crit}}{2.1 \times 10^{10} \ {\rm cm}^{-3}} \right)^{-1/2}. \tag{4}$$

Test simulations of spherical collapse and the simulation reported here confirm the appearance of first shocks at distances close to the above value.

We treated the propagation of radiation in the optically thick regime in the radiative diffusion limit (see Appendix A). We also incorporated dust properties such as the frequency independence of cooling at temperatures above 100 K, as well as the melting of dust grains at temperatures around 1500 K.

Finally, we included both the formation and dissociation of molecular hydrogen. The formation rate of H_2 molecules on dust surfaces was computed using the results of Hollenbach & McKee (1979). We used the dissociation rates of molecular hydrogen as computed in Shapiro & Kang (1987).

In order to understand the effects of these different processes in a dynamic calculation, we first ran a series of test simulations of the collapse of isolated, non-rotating, non-magnetized BE spheres. Fig. 2 shows the result of our BE collapse which include the process of H_2 dissociation (this simulation started with the assumption that the gas is completely molecular to begin with). As shown in Appendix A, the temperature in the radiation diffusion regime rises as $T \propto n^{1/3}$. At the density $n_{\rm cr} \sim 10^{16}$ cm^{-3}, the temperature reached $\sim$1200 K, which is hot enough to effectively dissociate hydrogen molecules. However, the subsequent reduction of the gas temperature reduces the dissociation efficiency leading to a self-regulated, slow, disintegration of hydrogen molecules over a wide range of densities.

We now turn to an analysis of the results of our turbulence simulations and the formation of massive stars.

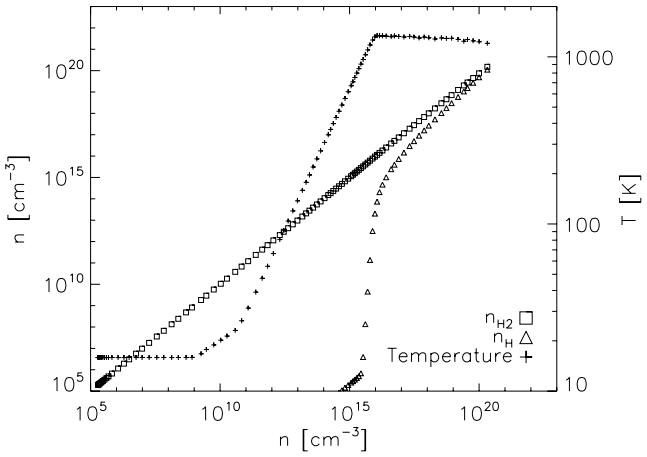

Figure 2. The evolution of the hydrogen densities and gas temperature of our non-rotating, non-magnetized collapse simulation. As predicted from our theoretical considerations, the dissociation of H_2 molecules is a *self-regulating* process over a wide range of densities. The efficient cooling from the dissociation process (see equation A28) reduces the gas temperature and subsequently slowing down the dissociation of H_2 molecules.

3 EVOLUTION OF THE LARGE-SCALE FILAMENTS

The initial state for our simulation, shown in Fig. 1 (a 3D version of this is rendered in fig. 7 of TP04), already shows that large-scale structure has formed in our simulation volume. Hundreds of lower mass cores are present in this volume, and as the virial analysis in that paper showed, many of the cores have started to collapse. The first core to violate the Truelove criterion in TP04 is the most massive core. As already noted, the oblique shocks which are responsible for the core formation are also responsible for the non-vanishing distribution of angular momenta in the cores. As we will see later, this initial spin results in a disc during the contraction phase. The AMR simulation zeros in on the evolution of the filamentary structure associated as it collapses to form a disc and protostar. The time-scale for the development of this non-linear, gravitationally dominated, structure is very fast – amounting to several thousand years. In this time frame, the larger filament scale remains fairly unaltered as material starts to drain into the assembling protostellar disc.

The forming accretion disc is deeply embedded in the much larger scale filament as is nicely shown in Fig. 3. The large-scale filament is about 2600 au in length and one sees the converging accretion flow on the 150-au scale view presented in the middle panel. On this intermediate 150-au scale, the disc grows within a filament that is developing out of a sheet-like structure. As we will see, the transfer of material from the sheet into the filament is associated with net angular momentum – and tends to resemble the growth of a large-scale, spinning vortex. The disc, forming on yet smaller scales, acquires this angular momentum from this larger scale process. We see the actual disc at this time in the right-hand panel, on a scale of only 37 au in diameter.

More details about the multiscale structure of this filament are shown in three figures (Figs 4–6). These represent three different 2D cuts through the simulation data at the end of our simulations. The structures are shown at increasingly resolved (finer) physical scales. Figs 4 and 5 feature cuts down the length of the filament which extends roughly along the vertical (z) axis (xz and yz planes, respectively). We clearly see a resolved filamentary structure on the largest scales (10^{17}–10^{16} cm) in the upper left-hand frame of the

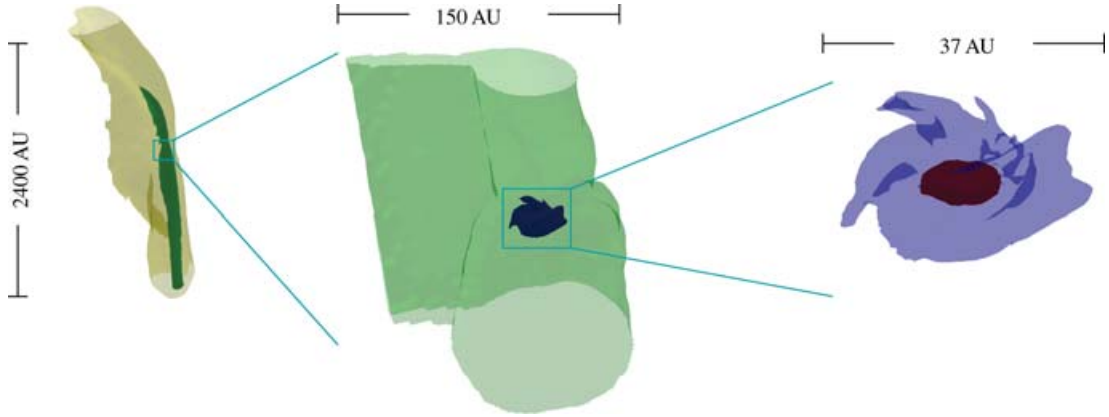

Figure 3. Density isosurfaces at different scales: 2400, 150 and 37 au. The panels show the large-scale filament, the protostellar disc within the filament and the inner region of the disc. The density isosurface shown in opaque green in the left-hand panel corresponds to the density shown in transparent green in the middle panel. Correspondingly, the opaque blue in the middle panel and the transparent blue in the right-hand panel show the same density isosurface.

picture. On the smallest scales (highest resolution), shown in the bottom right-hand panel, we see the formation of a disc.

Two kinds of large-scale velocity fields are shown in these figures.

(i) Flow of material into the filament from larger scales. This is a consequence of the large-scale velocity field associated with the original supersonic turbulence field (most of the power is on the largest scales – as in any general turbulent flow).

(ii) Large-scale flow of material along the filament that converges to form a disc near to its mass centre.

In the first case, the large-scale flow continues to shock the filament and maintains the high pressure within it preventing its dispersal. We have measured the pressure in the initial state of this filament to be of the order of $P/k_B \simeq 10^9$ K cm^{-3}, which is high but expected in a converging flow at Mach numbers of the order of 5. In the second case, the material in the filament undergoes gravitational collapse along the filament and towards the point of concentration – the disc.

We show the disc (edge-on) close-up in the bottom panels of Figs 4 and 5. The filamentary collapse flow undergoes a shock with the dense and slowly cooling gas, and material joins the forming disc. Given that this is a highly asymmetric, 3D simulation, it is interesting that this small-scale disc is not badly warped, although it cannot be described as being perfectly axisymmetric.

A top-down view of the forming disc, and another aspect of the accretion flow that is giving its life, is seen in Fig. 6. This crosscut (xy plane) through the mid-plane of the disc shows that material from the large-scale filament and the attached sheet is accreting on to the disc. Panel d of this figure especially shows an accreting structure that looks like a picture of accretion flow in a Roche overflow in a binary system. The disc at the highest resolution (Panel f) shows the presence of a bar, which is instrumental in driving a rather high accretion rate through the disc, as we will see.

While we do not follow the collapse of smaller regions in Fig. 1 in this paper, we know that filamentary structure is associated with low-mass cores as well (TP04). These varied filaments are the result of shocks on different physical scales and different intensities. This implies that the mass flow rates through them and on to their embedded cores would be very different. Thus, low-mass stars would also be expected to form through the filamentary accretion we study here.

4 DISC FORMATION

We present in Figs 7 and 8 a close-up snapshot of the temperature structure of the disc, on ∼16 -au scales. Fig. 7 shows the accretion shock very clearly. Material, raining into the disc from large-scale flows along the filament, shocks with the disc because the gas cannot cool quickly enough at these densities. One notes that rather high temperatures of the order of 1000 K are associated with this accretion shock which envelops the entire disc. The post-shock gas cools rather quickly, and is found at much more modest temperatures of 200–400 K. As demonstrated in Banerjee et al. (2004) and by others (e.g. Yorke, Bodenheimer & Laughlin 1995; Tomisaka 2002; Matsumoto & Tomisaka 2004), this cooler post-shocked gas gets re-accelerated and shocks again further into the gravitational potential resulting in a double (or multiple) shock structure of the accreting gas.

A top-down close-up of the disc's temperature distribution is shown in Fig. 8. We clearly see a well-resolved large-scale spiral wave pattern with two spiral arms (on 16-au scales) that appears to be attached to a bar at the centre of the disc. This is the state of the disc at the earliest times, long before the Class 0 phase has ended. The presence of this density wave is central to the rapid transport of disc angular momentum that we will examine later.

In order to understand what kind of emission one might expect from such a disc (in accordance with our radiation diffusion approximation), we present an optical depth map – which maps out values of the Rosseland mean opacity of the disc – as shown in the two panels of Fig. 9. We see the disc in edge-on as well as a top-down view. The post-shock gas is very dense and the grains give it a high optical depth ranging from $\tau \simeq 10^3$–10^6 in the dense regions on ∼10-au scales. One also sees that the spiral wave features seen in the temperature and density maps also show up in the optical depth maps of the disc's radial structure.

The evolution of the radial structure of the disc is shown in Figs 10 and 11.[2] In these very early and deeply embedded stages of disc and star formation, we find that the disc is actually more massive than the central protostellar object for a brief period. This is seen in the left-hand panel of Fig. 10 wherein the mass inside 1 au at the latest time is roughly 10^{-2} M$_\odot$, whereas the mass enclosed within 10 au

[2] These radial profiles show spherically averaged quantities with the centre at the peak density.

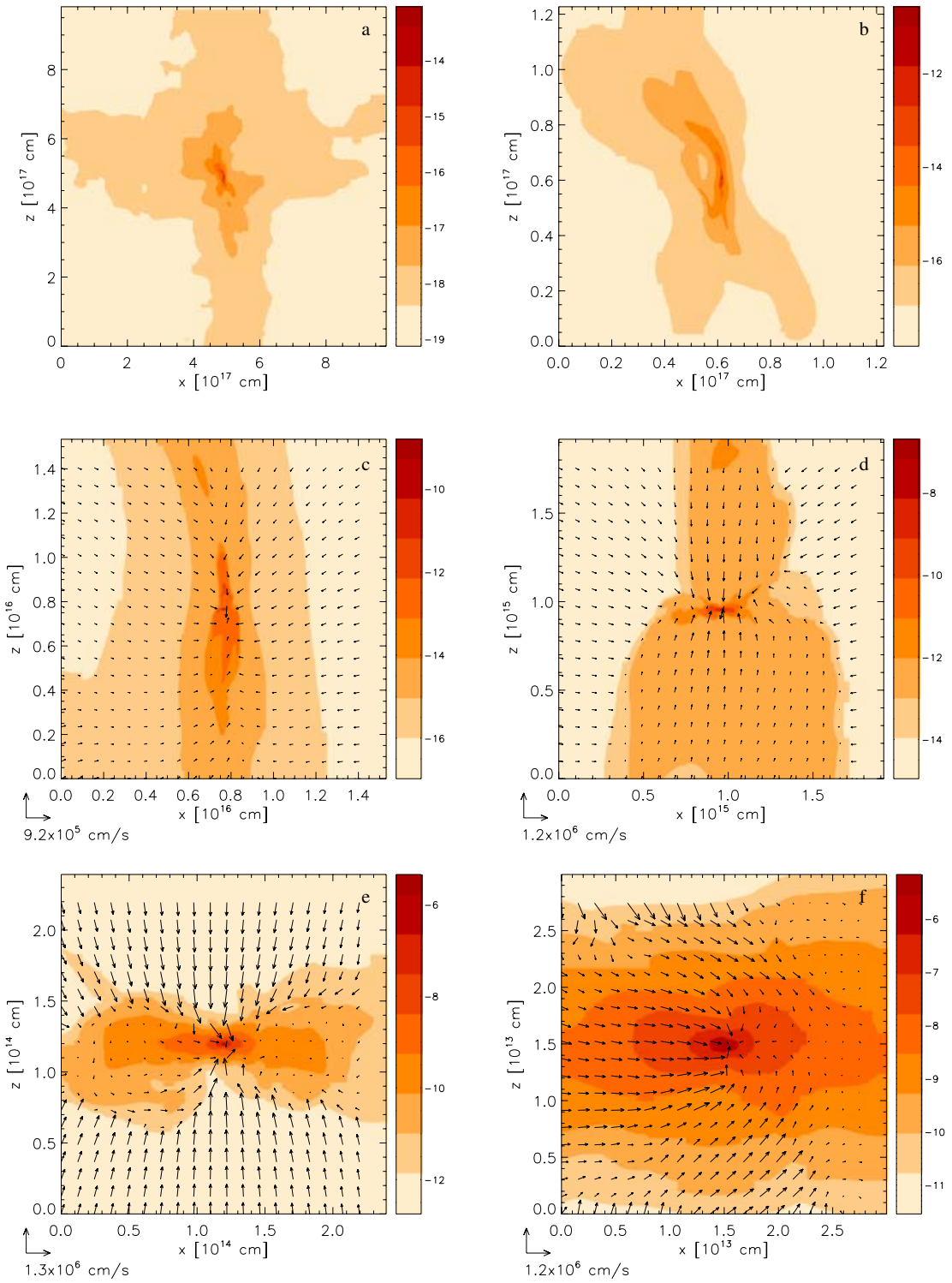

Figure 4. 2D slices of the matter density (logarithmic in grams per cubic centimetre) in the *xz* plane at different scales from the latest stage of our simulation. Panels a–f show the density structure on continuously smaller scales: 0.3 pc (a), 8.2×10^3 au (b), 1×10^3 au (c), 128 au (d), 16 au (e) and 2 au (f). These slices cut parallel through the filament and show the protostellar disc edge on. The arrows indicate the velocity field.

is about 10 times larger: $10^{-1}\,M_\odot$. Another interesting feature of this mass distribution is that the mass within the disc and protostar is a small fraction of the total mass that is distributed on larger scales. At 10^{17} cm, this amounts to a total of $13\,M_\odot$ while at a parsec scale, we have a total of 100 solar masses – reflecting the mass of the cluster-forming clump. This distribution of mass is very similar in character to simulations of the first star formed in the Universe (Abel, Bryan & Norman 2002). Although the cooling function of gas forming the first star is, of course, vastly different from later epochs that we are simulating here, nevertheless the two results both show

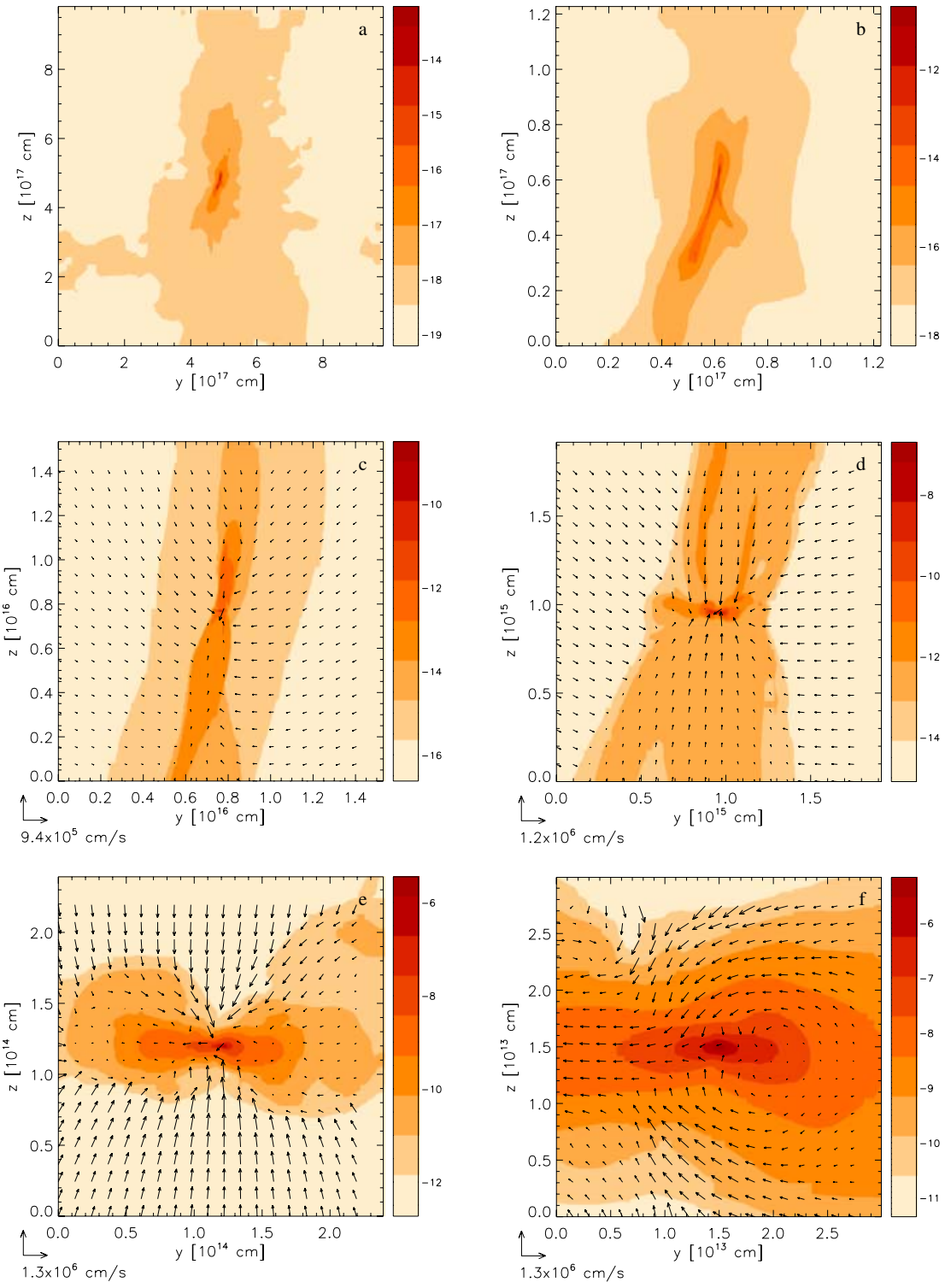

Figure 5. 2D slices of the matter density (logarithmic in grams per cubic centimetre) in the *yz* plane at different scales from the latest stage of our simulation. Panels a–f show the density structure on continuously smaller scales: 0.3 pc (a), 8.2×10^3 au (b), 1×10^3 au (c), 128 au (d), 16 au (e) and 2 au (f). These slices cut parallel through the filament and show the protostellar disc edge on. The arrows indicate the velocity field.

that massive stars are like the tips of icebergs in much more massive and extensive mass distributions.

The right-hand panel of Fig. 10 shows that the central density of the disc grows very rapidly with time. At each time, the run of density has a central, flat core radius (which size is of the order of the core's Jeans length) with a steeply falling density dependence beyond. Variations in the power-law slope arise because of the onset of different cooling rates of material at different densities.

The dominance of the disc over the protostellar mass at this early time does not violate any observations of disc-star systems since

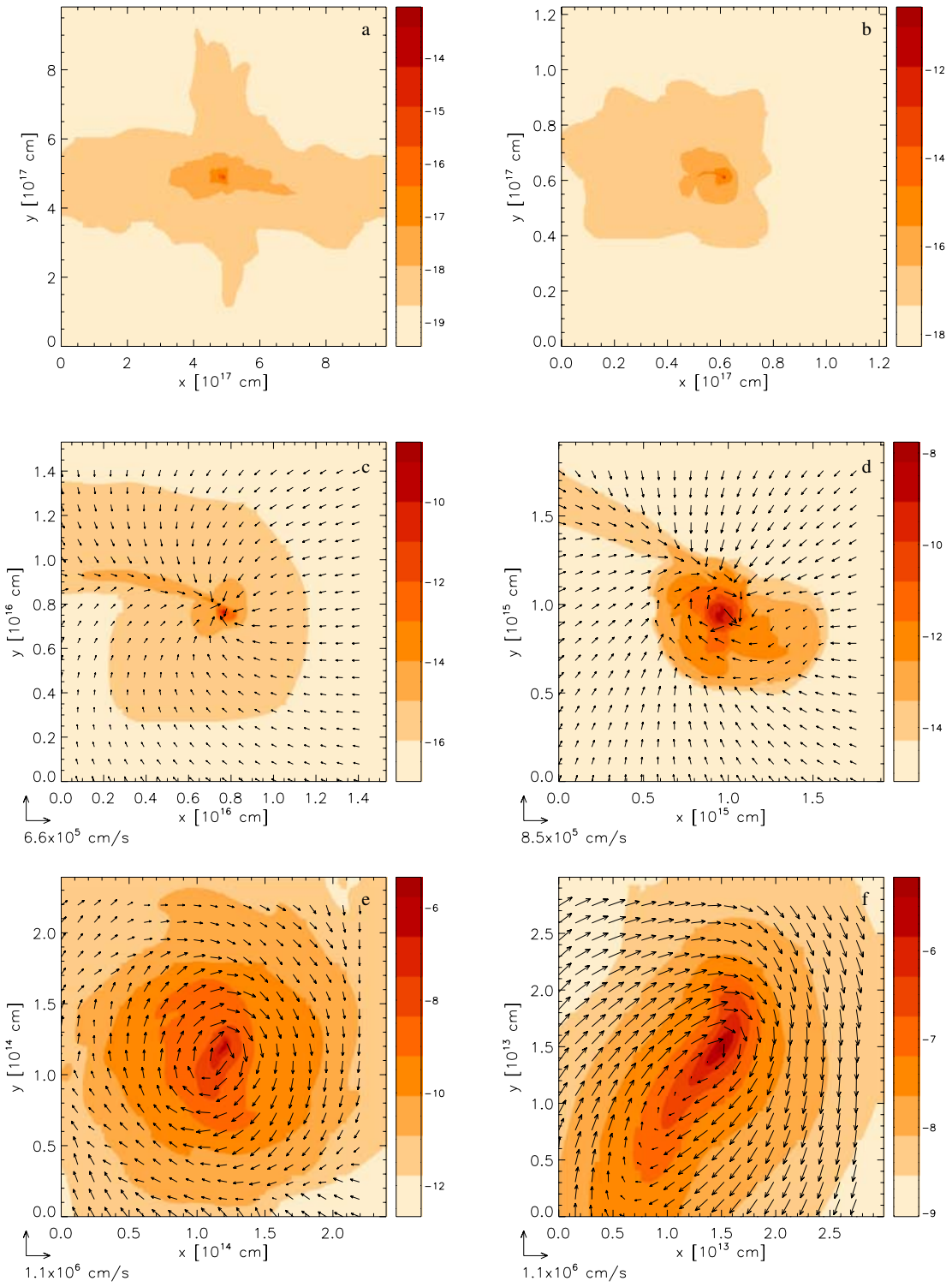

Figure 6. 2D slices of the matter density (logarithmic in grams per cubic centimetre) in the *xy* plane at different scales from the latest stage of our simulation. Panels a–f show the density structure on continuously smaller scales: 0.3 pc (a), 8.2×10^3 au (b), 1×10^3 au (c), 128 au (d), 16 au (e) and 2 au (f). These slices cut perpendicular through the filament and parallel through the disc plane. The thin sheet attached to the filament is also clearly seen in Panels c and d. The arrows indicate the velocity field.

the latter are generally available typically for Class I T-Tauri Stars and later. Theoretical calculations of disc formation often employ the assumption of self-similar collapse, in which the central object dominates the mass. We do not see this in our simulations. We also note that a dominant central mass does not appear in our earlier simulations of the hydrodynamic collapse of a Bonner–Ebert sphere (Banerjee et al. 2004).

Theoretical discussions of disc formation also often noted that discs needed to be lower in mass than their central stars; otherwise they would be out of equilibrium. This presents no problem to

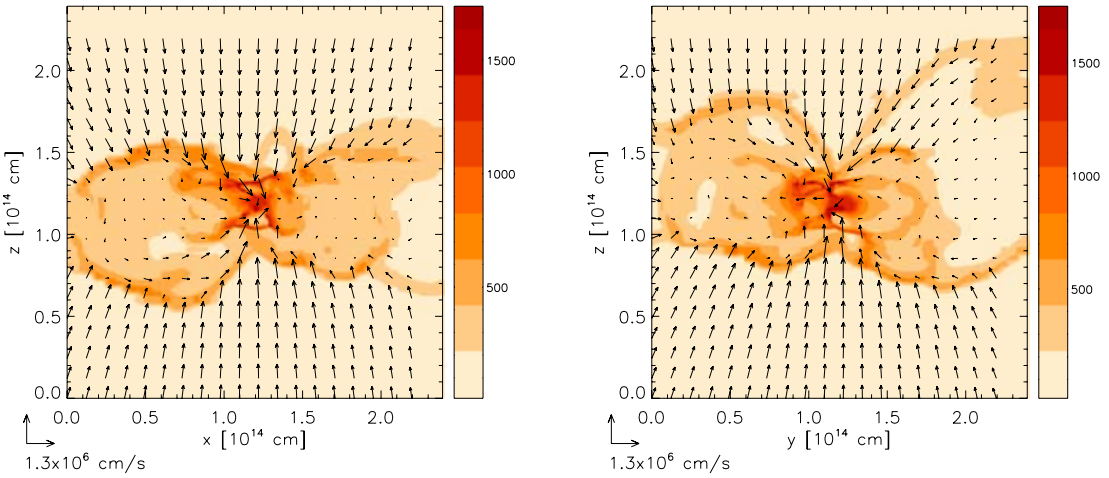

Figure 7. Temperature contours (in Kelvin) in the *xz* and *yz* planes which cut perpendicular to the disc plane (scale: ∼16 au). The first shocks appear in the region of the optically thin–optically thick transition. The arrows indicate the velocity field. The corresponding density maps are shown in Panel e of Figs 4 and 5, respectively.

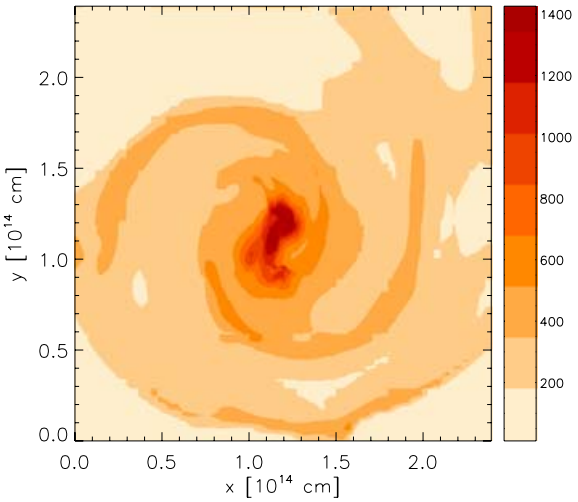

Figure 8. Temperature contours (in Kelvin) in the disc plane (*xy* plane) at ∼16-au scales. Clearly visible are the two arm spirals and the centre bar in this temperature map. The corresponding density map is shown in Panel e of Fig. 6.

these early systems. In fact, rapid stellar formation would be highly favoured if discs were more massive in their earlier stages. These highly unstable discs favour the appearance of high formation rates – which is what we will show later in this paper.

We also do not see further fragmentation of the protostellar disc at this stage. The increasing pressure of this optically thick disc stabilizes the disc against fragmentation. This shows again that the thermal evolution of the collapsing cloud core plays a crucial role in determining the fate of the protostellar system. For instance, molecular clouds will fragment easily in the regime where abundant molecular hydrogen is formed and subsequently the pressure decreases (e.g. Turner et al. 1995; Whitworth et al. 1995; Bhattal et al. 1998).

Fig. 11 summarizes the evolution of the disc's radial column density and temperature distributions. The outer regions of the disc beyond 10 au or so show a rather shallow column density profile, $\Sigma \propto r^{-1.25}$, compared to the minimum mass solar nebula. We also see that a high column density of $\simeq 10^3$ g cm^{-3} is achieved at about an au scale, which is then surpassed. We are charting the non-equilibrium early phase of disc formation and evolution just before the major delivery of mass into the central protostar has occurred. It is therefore not a surprise that transitory column densities in excess of the solar nebula model will arise. The radial temperature distribution in the disc scales as $T \propto r^{-1}$ at larger radii, with a flat distribution in the disc centre. This steep temperature profile reflects again the early stage during the assembly of the protostar where shocks from the infalling gas on to the adiabatic core are still present. It is interesting that while the envelope of this collapsing region features relatively smooth variations of the column and density profiles, the temperature profile falls steeply and then abruptly changes to the nearly isothermal background. This transition in disc temperature behaviour may be the best way of detecting the outer accretion shock and hence the outer disc edge.

The question of how angular momentum is distributed and transported in these early phases is arguably one of the most interesting and important issues for disc evolution and massive star formation. We plot, in the left-hand panel of Fig. 12, the specific angular momentum $j(r)$ (angular momentum per unit mass) as a function of disc radius for different times. We see, for all times after the initial state, that $j(r)$ is an increasing function of the disc radius. Rayleigh's theorem informs us that this is in fact a stable distribution of angular momentum (rotating bodies with constant or increasing specific angular momenta are stable). Only one graph is different; this corresponds to the initial state where we see a levelling of $j(r)$ at radii 10^{15}–10^{16} cm. Since the magneto rotational instability (MRI) is not present here, we must conclude that the bulk of the disc must be relatively free from turbulence in this early stage.

In the right-hand panel of Fig. 12, we replot this data in another interesting way – now showing the specific angular momentum as a function of the mass enclosed. This is a good way of measuring how much angular momentum is extracted and transported away from the enclosed mass (e.g. Abel et al. 2002). The figure shows that the specific angular momentum of material within the 0.01 $M_\odot$ mass shell has quickly lost nearly three orders of magnitude of specific angular momentum, having fallen from an initial value of 10^{20} cm^2 s^{-1} to about 10^{18} cm^2 s^{-1} in only 2400 yr. This angular momentum transport is achieved by the spiral waves that we have

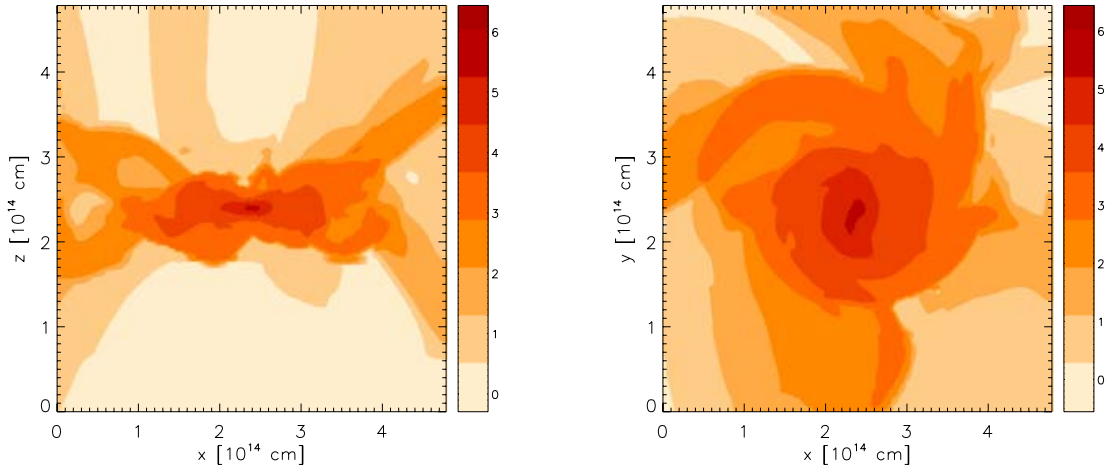

Figure 9. Optical depth (τ logarithmic see equation 2) perpendicular to the disc plane (left-hand panel) and in the disc plane (right-hand panel) at ∼32-au scales. The optical depth varies over six orders of magnitude within the protostellar disc and resembles its spiral structure.

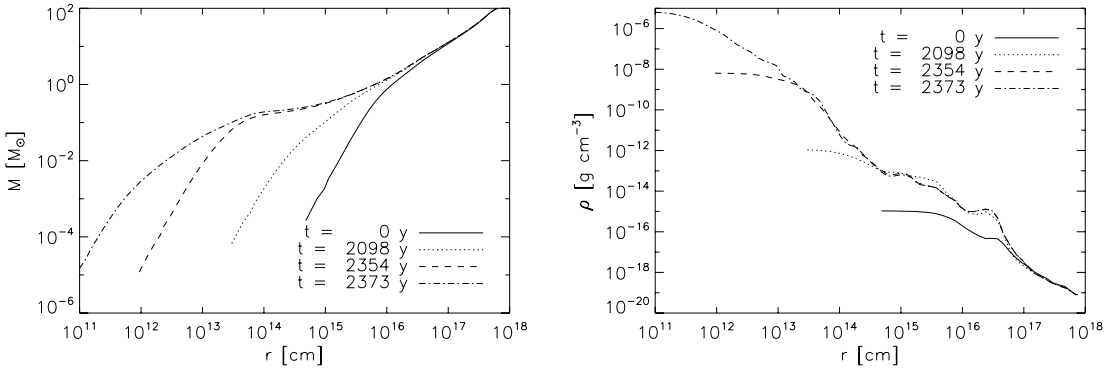

Figure 10. Radial profiles of the enclosed mass and mass density at different times. The $t = 0$ yr graph shows the profile at the beginning of our simulation run, and the subsequent labels indicate the time past since then.

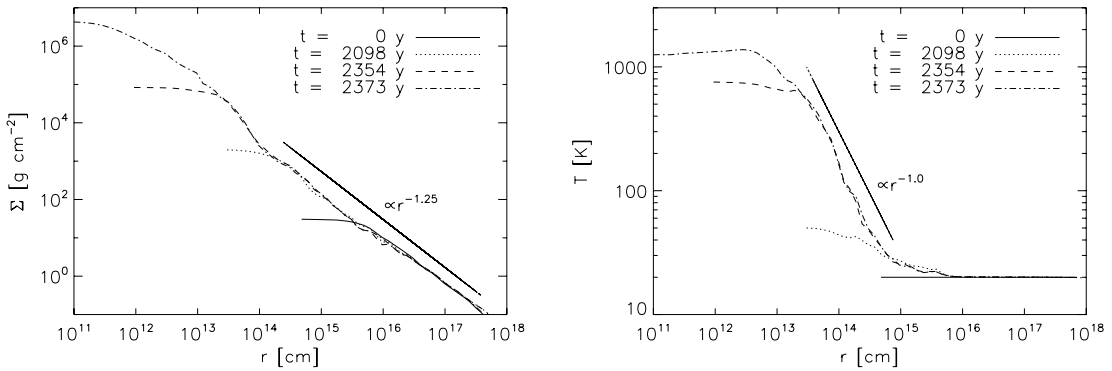

Figure 11. Radial profiles of the surface density and temperature at different times. The $t = 0$ yr graph shows the profile at the beginning of our simulation run, and the subsequent labels indicate the time past since then.

seen in the earlier figures (Figs 6, 8 and 9). As is well known, spiral wave torques are very efficient in transporting disc angular momentum because of their long lever arm. In the absence of either outflows or turbulence (through the MRI instability that would be active in the presence of a magnetic field), the plot shows that the non-equilibrium disc is very efficient in generating a spiral wave structure that efficiently transports angular momentum out of the central disc.

We measure how far the disc is from a Keplerian distribution in Fig. 13. We normalize the measured rotation speed with the local Kepler velocity by using the mass in the interior radius. The left-hand panel of this figure shows that this disc rotates more slowly by a factor of about 2 than Keplerian value within several tens of au. There are several peaks in the value of the rotation speed suggesting that shock waves within the disc are active and may be playing a role in helping to redistribute disc angular momentum.

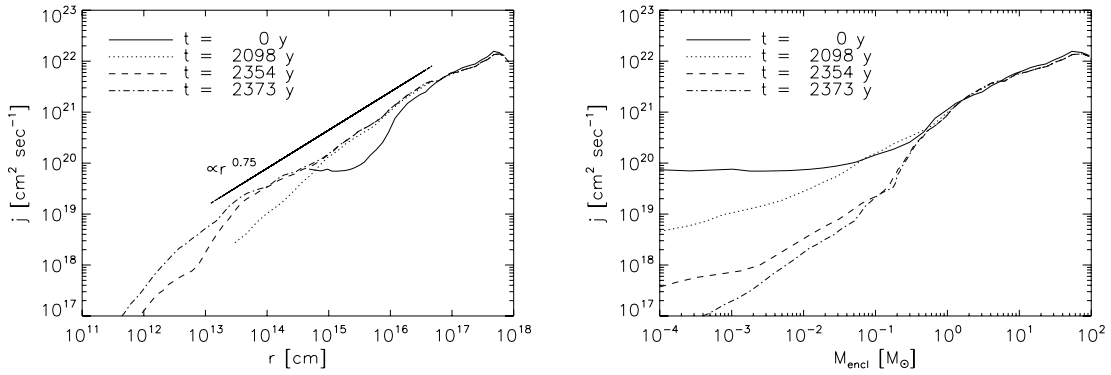

Figure 12. The evolution of the spherically averaged specific angular momentum as a function of radius (left-hand panel) and enclosed mass (right-hand panel). During the accretion phase, angular momenta are exchanged between 'mass shells'. The $t = 0$ yr graph shows the graphs at the beginning of our simulation run, and the subsequent labels indicate the time past since then.

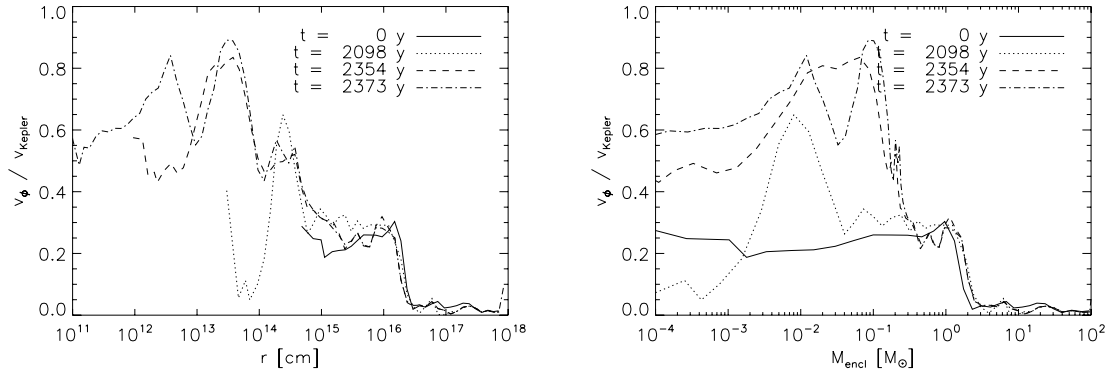

Figure 13. The evolution of the rotational velocity compared to the Keplerian velocity as a function of radius (left-hand panel) and enclosed mass (right-hand panel). The $t = 0$ yr graph shows the profile at the beginning of our simulation run, and the subsequent labels indicate the time past since then.

The right-hand panel of Fig. 13 shows that the rotation speed of enclosed mass shells increases quickly over the simulated time period which for the $0.1\,M_{\odot}$ mass shell doubles in spin from 1/3 to roughly 2/3 of its Kepler value. This reflects the growth in mass of the central protostellar core at the expense of disc material over this time period.

5 MASSIVE STAR FORMATION

Although we stopped our simulation at a very early stage into the formation of the central star (pre-Class 0 object), we speculate that this object will grow quickly to form a massive star since it is embedded in a massive envelope and the mass accretion is sufficiently high to overcome the radiation pressure from the burning young massive star. Most of the material that is destined to form the massive star in this simulation is assembled by channelling the material flowing along the spinning filament, through the accretion shock and into the star by accreting through the disc. Of greatest importance is the question of just how large the disc accretion rate is in these early phases.

We plot the spherically averaged, radial infall velocity as both a function of radius, as well as of enclosed mass, in Fig. 14 (left- and right-hand panels, respectively). The left-hand panel shows some of the characteristics of outside-in collapse that distinguish the collapse of Bonner–Ebert spheres. In the left-hand panel of this figure, we see that the core is already in a state of infall in the initial state of our simulation. The outer envelope has begun to collapse while most of the interior material is still nearly at rest. As the collapse develops, the core radius progressively shrinks as its density grows. At the same time, the maximum infall velocity continues to grow. The outside-in velocity structure is essentially the same as that seen in the collapse of Bonner–Ebert spheres, wherein the ever increasing density of the core is supplied by collapsing material in the envelope.

The collapsing gas eventually reaches a density, on small enough scales, that cooling is too slow and a shock is formed as the outer material arrives at the position of the more slowly contracting denser material. This happens first at a radial scale of a few 10^{14} cm. This is the well-known appearance of the first core, whose interior contracts almost adiabatically (e.g. Larson 1969). The 2D spatial cuts shown in Fig. 7 clearly show that this is indeed the scale of the first shock, where dust cooling in the optically thick regime has become too inefficient to prevent the appearance of a shock wave. This change in the cooling behaviour of the gas also appears as the change in density behaviour seen in the left-hand panel of Fig. 11. This scale can be predicted theoretically from the cooling function itself, as we have noted in previous papers (see e.g. Banerjee & Pudritz 2006).

Another interesting aspect of the collapse is that the infall speed is much higher than the original isothermal sound speed that characterizes the initial state, and reaches values of Mach 6 on 10^{15} cm scales. It is also higher than the asymptotic infall velocity of collapsing, isothermal Bonner–Ebert sphere where the Mach number reaches ∼3. The reason for the exceedingly high infall rate in our case is the initial supersonic turbulence. The right-hand panel of Fig. 14 shows the infall speed as a function of the mass enclosed.

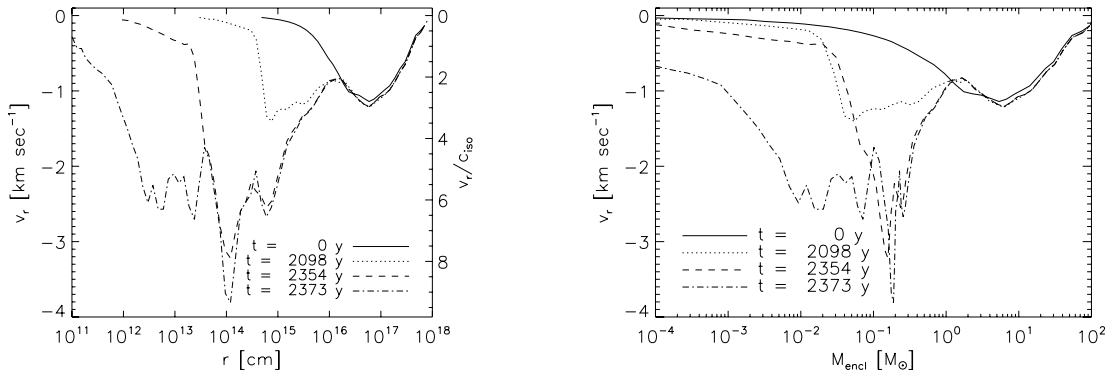

Figure 14. The evolution of the radial infall velocity as a function of radius (left-hand panel) and enclosed mass (right-hand panel). The collapse proceeds from outside-in resembling a collapsing Bonner–Ebert sphere. The $t = 0$ yr graph shows the profile at the beginning of our simulation run, and the subsequent labels indicate the time past since then.

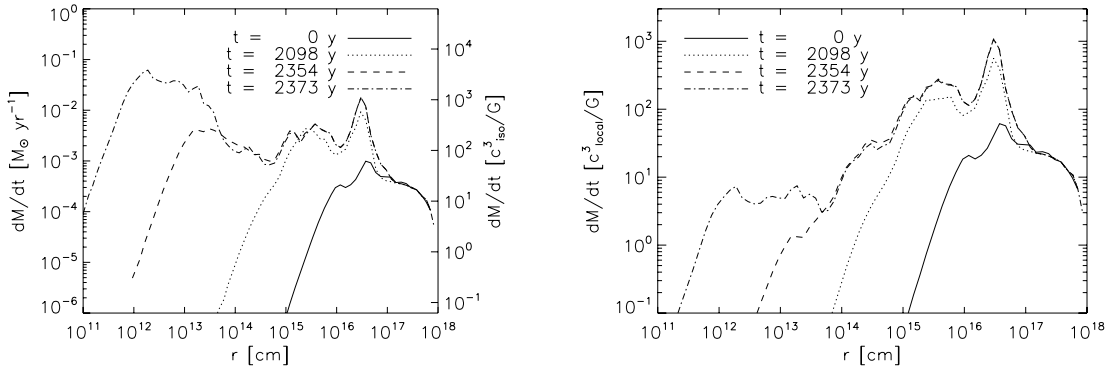

Figure 15. The evolution of the mass accretion through spherical shells around the core centre. The magnitude of the mass accretion is shown in absolute values and scaled to the isothermal quantity $c_{\rm iso}^3/G$ (left-hand panel), and scaled to the *local* $c_{\rm local}^3/G$ accretion measure (right-hand panel). The $t = 0$ yr graph shows the profile at the beginning of our simulation run, and the subsequent labels indicate the time past since then.

Only a small fraction of the infalling material reaches such high Mach number, typically less than 10 per cent at these early times.

Perhaps the most important aspect of filamentary accretion is in driving high accretion rates of material on to the disc. We show the spherically averaged accretion rates as a function of disc radius in the left-hand panel of Fig. 15, in both absolute terms, and then scaled with respect to the initial isothermal sound speed, $c_{\rm iso}$, of the gas at the beginning of the simulation. As expected from the velocity behaviour of the collapse shown in the previous Fig. 14, the accretion rate peaks at some radius, and this peak moves inwards with time to smaller and smaller scales. The initial state is already collapsing, as already noted and expected from the TP04 simulation. The peak of the mass accretion rate is located at the same radius at which the infall speed achieves its highest value (compare left-hand panels of Figs 14 and 15). Note that at 1 au the infall rate is several $10^{-3}\,{\rm M}_\odot\,{\rm yr}^{-1}$ which in the last frame is 10 times higher on sub-au scales. In terms of the initial isothermal sound speed of the simulation, the infall accretion rate has reached more than $10^3 c^3/G$! This value is about 1000 times higher than predicted by the self-similar solution of singular collapse (Shu 1977) and about 20 times higher than one would expect for Bonner–Ebert collapse, as first calculated by Penston (1969) and Larson (1969) (see also Hunter 1977).

The right-hand panel of Fig. 15 once again plots the accretion rate as a function of disc radius, except normalized with respect to *the local* sound speed, $c_{\rm local}^3/G$. This latter quantity is certainly not isothermal, and is the sound speed in the local gas that is undergoing the many cooling processes that we discuss in Appendix A. This local sound speed is of course greater than the initial isothermal sound speed that we start the simulation with because the gas heats substantially as a consequence of shocks. Thus, as the temperature rises towards the disc's interior the local sound speed increases as does the value of $c_{\rm local}^3/G$. In the last time plotted, the ratio of the infall rate to that computed from this local sound speed is only a factor of 10 larger at scales around 1 au.

6 DISCUSSION AND CONCLUSIONS

Our high-resolution simulations of a cluster-forming molecular clumps show that the formation of large-scale filaments plays a major role in the formation of accretion discs and massive stars. Our AMR technique tracked the collapse of the most massive structure which was the first to form in the cluster-forming clump which is our initial state. The rapid assembly of a massive star – at accretion rates that are an order of magnitude greater than analytic estimates – arises for two basic reasons: (i) supersonic turbulence rapidly sweeps up dense, large-scale structures by compressing a large volume of gas into sheets and filaments and (ii) the high accretion rates in filaments that features the flow of some material at unusually high Mach numbers.

6.1 Collapse in filaments

The cooling function for gas in the initial state dictates that the dusty molecular gas remains essentially isothermal until densities

of the order of 10^{10}–10^{11} cm^{-3}. The shock waves enormously compress the material by factors of the order of $\mathcal{M}^2$, where $\mathcal{M}$ is the Mach number. For our simulation, the initial rms Mach number (characterizing the entire turbulent spectrum) is 5, so that the forming molecular core in this filament has already had an enormous boost in its background density, and therefore background pressure.

The increase in gas density brought about by the shock then increases the infall rate in the filament by a large factor. Since the infall speed scales as $v_{\rm ff} \propto \rho^{1/2}$, we anticipate that gravitational collapse in such a filament is boosted by a factor of $v_{\rm ff} \propto \mathcal{M}$ over typical 'virial theorem' estimates.

We have also observed that the infall occurs in a fashion somewhat like the outside-in collapse of a Bonner–Ebert sphere. It is important to remember that a BE sphere collapse has an infall rate that is much larger than given only by the sound speed; one finds $\dot{M} \simeq f\, c^3/G$ where $f \simeq 20$–50 as was restated by Hunter (1977). We argue that the factor should scale as $f \simeq \mathcal{M}^3$, i.e. that one replaces the sound speed in the virial formula with the free-fall speed. Thus, since the detailed numerics show that a maximum infall speed of $\mathcal{M} \simeq 6$ is reached, then $f \simeq 216$. This value gets us into the right regime but is still not the factor of 10^3 enhancement that we see in the most extreme case in our. The difference could be due to a combination of factors including a geometric factor.

The point is that the filamentary collapse delivers an accretion rate that is greatly in excess of what is needed to create a massive star in the conditions, on time-scales of only a few thousand years from the point where these filamentary initial conditions have been created.

6.2 Role of cooling

Cooling plays an important role in these processes, because it ultimately controls how dense structures can become. As long as the gas is isothermal, it can become highly compressed as a consequence of shock waves. This early isothermal phase lasts until the gas starts to become optically thick to emission from dust, at densities exceeding 10^{11} cm^{-3}. At this density, gas becomes optically thick to dust cooling and begins to contract quasi-adiabatically. This scale is the characteristic of the first shock that appears at 10–20 au (see Fig. 7) that defines the disc envelope.

The second density of importance is at 10^{16} cm^{-3} at which molecular hydrogen begins to dissociate. We find that an interesting, self-regulated state arises in which the gas is kept just cool enough to avoid both the total dissociation of molecular hydrogen, as well as the preservation of dust grains from evaporating. Molecular hydrogen cooling regulates the gas temperature. The dissociation of molecular hydrogen is important because it allows the collapse to resume, as has been noted by many authors (e.g. Larson 1969).

6.3 Conclusions

Our basic conclusions are as follows.

(i) The assembly of protodiscs and protostars is a rapid process in a supersonic, turbulent environment.

(ii) The most massive object forms first within the molecular cloud was the first to violate the Truelove condition in our simulation. This raises the question of how feedback from this (massive) star will affect the collapse and star formation in the many other smaller cores that formed in our simulation.

(iii) The collapse proceeds from outside-in where the accretion through the large-scale structure (a filament in our case) 'feeds' the dense protostellar structure within it.

(iv) The initial spin of the filament from oblique shocks lead to disc formation because of efficient dust cooling until densities of $\sim 10^{11}$ cm^{-3}.

(v) Even in the absence of magnetic fields and/or outflows angular momentum is transferred very efficiently through spiral waves in the disc.

(vi) We observe very high accretion rates ($\dot{M} \sim 10^{-2}$ M$_\odot$ yr^{-1}) due to filamentary accretion of the supersonic gas on to the forming discs. These rates are 10^3 times larger than predicted by the collapse of singular isothermal spheres. We find that a reasonable scaling for filamentary accretion is $\dot{M} \simeq f\, c^3/G$, where the pre-factor should scale as $f \simeq \mathcal{M}^3$, i.e. that one replaces the sound speed in the virial formula with the free-fall speed. Even this does not quite account for the full effect, and there is an additional factor of the order of a few that likely is geometric in nature and accounts for filamentary, rather than spherical infall geometry.

ACKNOWLEDGMENTS

We thank Debra Shepherd and James Wadsley for valuable comments on our manuscript. RB thanks Simon Glover for instructive discussions on microphysical processes. The FLASH code was in part developed by the DOE-supported Alliances Center for Astrophysical Thermonuclear Flashes (ASCI) at the University of Chicago. Our simulations were carried out on clusters of the SHARCNET HPC Consortium of Ontario. REP is supported by the Natural Sciences and Engineering Research Council of Canada.

REFERENCES

Abel T., Bryan G. L., Norman M. L., 2002, Sci, 295, 93
Alves J. F., Lada C. J., Lada E. A., 2001, Nat, 409, 159
Ballesteros-Paredes J., Klessen R. S., Mac Low M.-M., Vázquez-Semadeni E., 2006, in Reipurth B., Jewitt D., Keil K., eds, Protostars and Planets V. Univ. Arizona Press, Tucson, in press
Balsara D., Ward-Thompson D., Crutcher R. M., 2001, MNRAS, 327, 715
Banerjee R., Pudritz R. E., 2006, ApJ, 641, 949
Banerjee R., Pudritz R. E., Holmes L., 2004, MNRAS, 355, 248
Beuther H., Churchwell E. B., McKee C. F., Tan J. C., 2006, in Reipurth B., Jewitt D., Keil K., eds, Protostars and Planets V. Univ. Arizona Press, Tucson, in press
Bhattal A. S., Francis N., Watkins S. J., Whitworth A. P., 1998, MNRAS, 297, 435
Bonnor W. B., 1956, MNRAS, 116, 351
Dobbs C. L., Bonnell I. A., Clark P. C., 2005, MNRAS, 360, 2
Ebert R., 1955, Z. Astrophys., 37, 217
Elmegreen B. G., Scalo J., 2004, ARA&A, 42, 211
Falgarone E., Lis D. C., Phillips T. G., Pouquet A., Porter D. H., Woodward P. R., 1994, ApJ, 436, 728
Fiege J. D., Johnstone D., Redman R. O., Feldman P. A., 2004, ApJ, 616, 925
Fryxell B. et al., 2000, ApJS, 131, 273
Goldsmith P. F., 2001, ApJ, 557, 736
Hillenbrand L. A., 1997, AJ, 113, 1733
Hollenbach D., McKee C. F., 1979, ApJS, 41, 555
Hunter C., 1977, ApJ, 218, 834
Johnstone D., Bally J., 1999, in Ossenkopf V., Stutzki J., Winnewisser G., eds, The Physics and Chemistry of the Interstellar Medium. GCA-Verlag, Herdecke, p. 180
Klessen R. S., Burkert A., 2000, ApJS, 128, 287
Larson R. B., 1969, MNRAS, 145, 271
Lepp S., Shull J. M., 1983, ApJ, 270, 578

Low C., Lynden-Bell D., 1976, MNRAS, 176, 367
Mac Low M.-M., Klessen R. S., 2004, Rev. Mod. Phys., 76, 125
McKee C. F., Tan J. C., 2003, ApJ, 585, 850
McLaughlin D. E., Pudritz R. E., 1997, ApJ, 476, 750
Matsumoto T., Tomisaka K., 2004, ApJ, 616, 266
Mitchell G. F., Johnstone D., Moriarty-Schieven G., Fich M., Tothill N. F. H., 2001, ApJ, 556, 215
Neufeld D. A., Lepp S., Melnick G. J., 1995, ApJS, 100, 132
Olson K. M., MacNeice P., Fryxell B., Ricker P., Timmes F. X., Zingale M., 1999, BAAS, 31, 1430
Padoan P., 1995, MNRAS, 277, 377
Padoan P., Nordlund Å., 2002, ApJ, 576, 870
Palla F., Salpeter E. E., Stahler S. W., 1983, ApJ, 271, 632
Penston M. V., 1969, MNRAS, 145, 457
Porter D. H., Pouquet A., Woodward P. R., 1994, Phys. Fluids, 6, 2133
Semenov D., Henning T., Helling C., Ilgner M., Sedlmayr E., 2003, A&A, 410, 611
Shapiro P. R., Kang H., 1987, ApJ, 318, 32
Shu F. H., 1977, ApJ, 214, 488
Shu F. H., Adams F. C., Lizano S., 1987, ARA&A, 25, 23
Silk J., 1977, ApJ, 214, 718
Stone J. M., Norman M. L., 1992a, ApJS, 80, 753
Stone J. M., Norman M. L., 1992b, ApJS, 80, 791
Teixeira P. S., Lada C. J., Alves J. F., 2005, ApJ, 629, 276
Tilley D. A., Pudritz R. E., 2004, MNRAS, 353, 769 (TP04)
Tomisaka K., 2002, ApJ, 575, 306
Truelove J. K., Klein R. I., McKee C. F., Holliman J. H., Howell L. H., Greenough J. A., 1997, ApJ, 489, L179
Turner N. J., Stone J. M., 2001, ApJS, 135, 95
Turner J. A., Chapman S. J., Bhattal A. S., Disney M. J., Pongracic H., Whitworth A. P., 1995, MNRAS, 277, 705
von Weizsäcker C. F., 1951, ApJ, 114, 165
Whitworth A. P., Chapman S. J., Bhattal A. S., Disney M. J., Pongracic H., Turner J. A., 1995, MNRAS, 277, 727
Wolfire M. G., Cassinelli J. P., 1987, ApJ, 319, 850
Yorke H. W., Bodenheimer P., Laughlin G., 1995, ApJ, 443, 199

APPENDIX A: COOLING

In this appendix, we summarize the cooling processes which we included in our simulation.

A1 Molecular cooling

As in Banerjee et al. (2004) and Banerjee & Pudritz (2006), we include cooling by molecular line emissions calculated by Neufeld et al. (1995). These processes are most important in the low-density/low-temperature regime. In Banerjee et al. (2004), we showed that the collapse will proceed isothermally until $n \sim 10^{7.5}\,\mathrm{cm}^{-3}$ if only molecular cooling is considered.

A2 Dust cooling

Cooling by gas–dust energy transfer in the optically thin regime. Here, we follow the treatment by Goldsmith (2001) with the gas–dust energy exchange rate

$$\Lambda_{\rm gd} = 2 \times 10^{-33} \left[\frac{n(\mathrm{H}_2)}{\mathrm{cm}^{-3}}\right]^2 \left(\frac{\Delta T}{\mathrm{K}}\right) \left(\frac{T_{\rm gas}}{10\,\mathrm{K}}\right)^{1/2} \mathrm{erg\ cm^{-3}\ s^{-1}}, \quad \text{(A1)}$$

where $\Delta T = T_{\rm gas} - T_{\rm dust}$. This cooling process is very efficient until the core becomes optically thick.

We calculate the dust equilibrium temperature at each time-step by solving

$$\Gamma_{\rm cr} + \Lambda_{\rm gd} - \Lambda_{\rm dust} = 0 \quad \text{(A2)}$$

to get the self-consistent dust temperature. In the above equation, $\Gamma_{\rm cr}$ and $\Lambda_{\rm dust}$ are the heating by cosmic rays and the energy loss by dust (blackbody) radiation, respectively. As long as $\Delta T > 0$, the dust is also heated by the gas–dust interactions. The heating rate by cosmic rays is (Goldsmith 2001)

$$\Gamma_{\rm cr} = 3.9 \times 10^{-28} \left[\frac{n(\mathrm{H}_2)}{\mathrm{cm}^{-3}}\right] \mathrm{erg\ cm^{-3}\ s^{-1}}, \quad \text{(A3)}$$

where we assume a shielding parameter of $\chi = 10^{-4}$.

A2.1 Optically thin regime

The dust grains lose their thermal energy by blackbody-like radiation:

$$\Lambda_{\rm dust} = \kappa\, \tilde{\sigma}\, T_{\rm dust}^4, \quad \text{(A4)}$$

where κ is the opacity (in cm^{-1}) and $\tilde{\sigma} = f\sigma$ is, up to a factor of the order of unity, the Stefan–Boltzmann constant σ. Using the values from Goldsmith (2001),

$$\kappa = 3.3 \times 10^{-26} \left[\frac{n(\mathrm{H}_2)}{\mathrm{cm}^{-3}}\right] \left(\frac{T_{\rm dust}}{18.24\,\mathrm{K}}\right)^2 \mathrm{cm}^{-1}, \quad \text{(A5)}$$

$$\tilde{\sigma} = 6.85 \times 10^{-5}\ \mathrm{erg\ cm^{-2}\ s^{-1}\ K^{-4}} = 1.209\sigma, \quad \text{(A6)}$$

the dust energy loss is

$$\Lambda_{\rm dust} = 6.8 \times 10^{-33} \left[\frac{n(\mathrm{H}_2)}{\mathrm{cm}^{-3}}\right] \left(\frac{T_{\rm dust}}{1\,\mathrm{K}}\right)^6 \mathrm{erg\ cm^{-3}\ s^{-1}}. \quad \text{(A7)}$$

Solving the dust equilibrium equation (A2), we find that the dust temperature, $T_{\rm dust}$, approaches the gas temperature, $T_{\rm gas}$, at densities $n(\mathrm{H}_2) \gtrsim 10^{7-8}\,\mathrm{cm}^{-3}$ depending on the initial gas temperature.

When the dust temperature is close to equal to the gas temperature, the effective gas cooling becomes

$$\Lambda_{\rm gd} \rightarrow \Lambda_{\rm dust}(T_{\rm dust} = T_{\rm gas}), \quad \text{(A8)}$$

where the dust temperature is replaced by the gas temperature. In this regime, one can estimate the effective equation of state (EoS) by equating the compressional heating with the above cooling:

$$\frac{\frac{3}{2}nkT}{t_{\rm ff}} = \kappa\tilde{\sigma}T_{\rm gas}^4, \quad \text{(A9)}$$

where $t_{\rm ff} = \sqrt{3\pi/32G_N\rho}$ is the free-fall time and $T_{\rm dust}$ is replaced by $T_{\rm gas}$ in κ. From equation (A9), we see that $n \propto T^{10}$ which results in an effective adiabatic index, i.e. $\gamma_{\rm eff} = 1 + \mathrm{d}\ln T/\mathrm{d}\ln n$, of

$$\gamma_{\rm eff} = \frac{11}{10}, \quad \text{when} \quad T_{\rm dust} \sim T_{\rm gas}. \quad \text{(A10)}$$

This result shows that the dust is still a very efficient coolant even if the dust temperature becomes almost equal to the gas temperature. We summarize the temperature trajectory and the evolution of the effective EoS in Figs 2 and A1 which show the result of one of our non-rotating, non-magnetized, spherical collapse simulations. The simulation results confirm the existence of the transition region from the isothermal collapse to $\gamma_{\rm eff} = 1.1$ at densities $n \gtrsim 10^9\,\mathrm{cm}^{-3}$.

A2.2 Optically thick regime

We treat the propagation of the radiation field in the optically thick regime, i.e. $\tau > 1$ (see Section 2.2, for our definition of the optical

depth τ), as a diffusion process using the following approximation. The energy loss carried by the radiation flux $\boldsymbol{F}$ is

$$\Lambda_{\rm rad} = -\nabla \cdot \boldsymbol{F}. \tag{A11}$$

In the Eddington approximation, the flux can be written as (e.g. Turner & Stone 2001)

$$\boldsymbol{F} = -\frac{c}{3\kappa}\,\nabla E, \tag{A12}$$

where c is the speed of light and $E = a_{\rm rad}\,T_{\rm dust}^4$ ($a_{\rm rad} = \frac{4\sigma}{c} = 7.565 \times 10^{-15}$ erg cm^{-3} K^{-4}) is the radiation energy associated with the dust.

In accordance with the approximation of the optical depth, equation (2), we use the Jeans length, $\lambda_{\rm J}$, as the typical length-scale over which the radiation field changes significantly. This allows us to approximate $\nabla \approx f/\lambda_{\rm J}$ and write equation (A11) as[3]

$$\Lambda_{\rm rad} \approx \frac{4}{3}\,f^2\,\frac{\sigma\,T_{\rm dust}^4}{\kappa\,\lambda_{\rm J}^2} \quad \text{(optically thick regime)}. \tag{A13}$$

We note that the local treatment of the radiation energy loss, equation (A13), is a good approximation in an ongoing collapse situation where the Jeans length is the dominant scale of the system. The approximation becomes less accurate in a system which is governed by different independent length-scales, as an equilibrium disc with a scaleheight h.

The expression in equation (A13) sets an upper limit of the radiation loss in the optically thick regime, and the dust cooling (equation A4) is determined by

$$\Lambda_{\rm dust} = \Lambda_{\rm rad} \tag{A14}$$

which leads to the replacement of the dust opacity in the optically thick regime

$$\kappa \rightarrow \tilde{f}/\lambda_{\rm J} \quad \text{(optically thick regime)}, \tag{A15}$$

where $\tilde{f} = \sqrt{4\sigma/3\tilde{\sigma}}\,f \approx 1.05\,f$.

In summary, we determine the dust temperature in the optically thin *and* optically thick regime by solving equation (A2) (using an iterative Newton method) with

$$\Lambda_{\rm dust} = \kappa_{\rm eff}\,\tilde{\sigma}\,T_{\rm dust} \tag{A16}$$

with

$$\kappa_{\rm eff} \equiv \min\left(\kappa,\,\tilde{f}\,\lambda_{\rm J}^{-1}\right). \tag{A17}$$

The cooling in the optically thick regime is less efficient than in the optically thin regime. Therefore, the time-scale which governs the evolution of the core becomes larger than the dynamical time-scale of the core region and is given by the cooling time

$$t_{\rm evol} = t_{\rm cool} = \frac{\frac{3}{2}\,n\,kT}{\tilde{\sigma}\,T^4\,\tilde{f}/\lambda_{\rm J}} = 2.1\,\tilde{f}^{-1}\left[\frac{n({\rm H}_2)}{10^{10}\ {\rm cm}^{-3}}\right]^{1/2}\left(\frac{T}{100\ {\rm K}}\right)^{-5/2}\ {\rm yr}. \tag{A18}$$

In Fig. A2, we show the density dependence of the core evolution time, $t_{\rm evol,sim} \equiv n/\dot{n}$ from our simulation and the time-scale from equation (A18). Both time-scales have the same dependence on density ($\propto n^{-1/3}$) in the optically thick regime and the same amplitude if we choose $\tilde{f} = 1.67$.

Equation (A18) does not constrain the density–temperature relation (i.e. the EoS). However, as the system collapses on a trajectory at which the thermal pressure is (almost) in balances with gravity, this trajectory will be the path at which

$$\gamma_{\rm eff} = \gamma_{\rm crit} = 4/3. \tag{A19}$$

Figs A1 and A2 show the evolution of the effective EoS ($\gamma_{\rm eff} = {\rm d}\ln p/{\rm d}\ln\rho$) and the temperature of the core region of our spherical collapse simulation. The collapse in the optically thick regime follows the path where $\gamma_{\rm eff} \approx \gamma_{\rm crit}$.

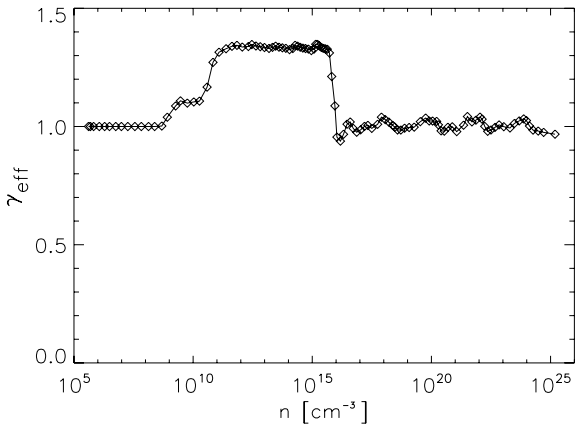

Figure A1. The effective EoS as a function of density from our non-rotating, non-magnetized spherical, collapse simulation in the case where dust cooling and H_2 dissociation are included. Clearly, two distinct transitions can be identified: at a density of $\sim 10^{11}$ cm^{-3} the core becomes optically thick and contracts on quasi-static trajectory, and at $\sim 10^{16}$ cm^{-3} H_2 dissociation becomes effective whereby slightly cooling the core region.

A3 Warm temperature regime and dust melting

At temperatures of about 100 K the dust opacity becomes almost independent of the frequency, and at temperatures around 1500 K the dust opacity decreases sharply due to the melting of dust grains (for a recent compilation of opacities, see Semenov et al. 2003). To incorporate these effects, we fit the dust opacity by a piecewise

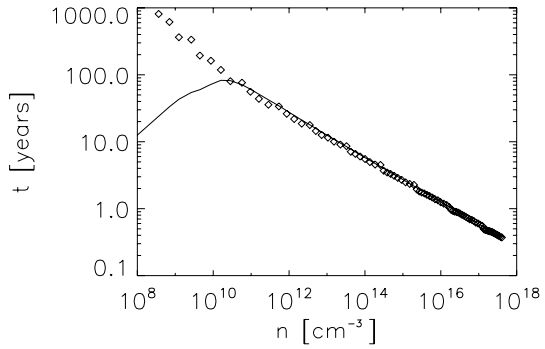

Figure A2. The evolution time of the density, i.e. $t_{\rm evol} = n/\dot{n}$ (diamonds) from our simulation and the time calculated from the prediction equation (A18) (line) where we set $\tilde{f} = 1.67$. The simulation follows closely the trajectory of our theoretical estimate of equation (A18).

[3] The factor f could be a function of density and temperature which can be determined by comparing simulation results using the diffusion approach, i.e. equations (A11) and (A12), with results using equation (A13). Here, we use a constant value which we determine by the comparison of equation (A18) with the results of our collapse simulation of a non-rotating, non-magnetized Bonnor–Ebert sphere.

power law (see also equation A5)

$$\kappa \propto \begin{cases} T^2, & T < 200\ \mathrm{K} \\ T^0, & 200\ \mathrm{K} < T < 1500\ \mathrm{K} \\ T^{-12}, & T > 1500\ \mathrm{K}. \end{cases} \quad \text{(A20)}$$

A4 H_2 formation and dissociation

We use the Hollenbach & McKee (1979) rates to account for the formation of H_2. These authors compute the formation of hydrogen molecule on dust grain surfaces from collisions with atomic hydrogen. The formation coefficient, R_f, can be written as

$$R_f = 3 \times 10^{-18} \times \frac{T^{1/2}\, f_a}{1 + 0.04\,(T + T_{dust})^{1/2} + 2 \times 10^{-3}\, T + 8 \times 10^{-8}\, T^2}, \quad \text{(A21)}$$

where T and T_{dust} are given in K and the factor f_a is given by

$$f_a = \frac{1}{1 + 10^4\, \exp(-600/T)}. \quad \text{(A22)}$$

To account for the process of H_2 dissociation in the hot dense region, we use the dissociation rates from Shapiro & Kang (1987) which are recalculated functions based on the work by Lepp & Shull (1983). These dissociation rates are calculated from the collisional break up of molecular hydrogen out of all 15 vibrational levels.

The dissociation rate coefficient can be well fitted to the form

$$\log k_D(n, T) = \log k_H - \frac{\log k_H/k_L}{1 + n/n_{tr}}, \quad \text{(A23)}$$

where k_D is given in units $\mathrm{cm^3\ s^{-1}}$ and k_H and k_L are the coefficients for the low- and high-density regimes, respectively,

$$\begin{aligned} k_L &= 1.12 \times 10^{-10}\, \exp(-7.035 \times 10^4\ \mathrm{K}/T)\ \mathrm{cm^3\ s^{-1}}; \quad \mathrm{H\text{–}H_2} \\ &= 1.18 \times 10^{-10}\, \exp(-6.950 \times 10^4\ \mathrm{K}/T)\ \mathrm{cm^3\ s^{-1}}; \quad \mathrm{H_2\text{–}H_2} \end{aligned} \quad \text{(A24)}$$

$$\begin{aligned} k_H &= 1.20 \times 10^{-9}\, \exp(-5.24 \times 10^4\ \mathrm{K}/T)\ \mathrm{cm^3\ s^{-1}}; \quad \mathrm{H\text{–}H_2} \\ &= 1.30 \times 10^{-9}\, \exp(-5.33 \times 10^4\ \mathrm{K}/T)\ \mathrm{cm^3\ s^{-1}}; \quad \mathrm{H_2\text{–}H_2}. \end{aligned} \quad \text{(A25)}$$

The transitional density n_{tr} in units of $\mathrm{cm^{-3}}$ is given by

$$\begin{aligned} \log n_{tr} &= 4.00 - 0.416\, x - 0.327\, x^2; \quad \mathrm{H\text{–}H_2} \\ &= 4.845 - 1.3\, x + 1.62\, x^2; \quad \mathrm{H_2\text{–}H_2} \end{aligned} \quad \text{(A26)}$$

with

$$x = \log T/10^4\ \mathrm{K}. \quad \text{(A27)}$$

The binding energy of H_2 molecules is 4.48 eV. For each collision with molecular hydrogen, which leads to its dissociation, this energy is lost from the (hydrogen) gas. Therefore, the effective cooling rate due to hydrogen dissociation is given by

$$\Lambda_{diss} = 4.48\ \mathrm{eV}\, n\, n(H_2)\, k_D, \quad \text{(A28)}$$

where n is either $n(H_2)$ or $n(H)$ depending on the collisional partner.

The FLASH code provides data arrays which store the mass, X_i, fraction of different species. We use this ability to keep track of the number densities of hydrogen in its different forms (i.e. molecular or atomic). The number density of the species i is given by

$$n_i = X_i\, \frac{\rho}{\mu_i\, m_H}, \quad \text{(A29)}$$

where μ_i is the atomic weight of the species i, ρ is the total matter density and m_H is the hydrogen mass.

We point out that we did not include effects from H_2 formation by three-body processes which could still be important in the high density ($>10^{16}\,\mathrm{cm^{-3}}$) and warm temperature ($<1100\,K$) regime. We might therefore slightly overestimate the cooling ability from H_2 dissociation. Three-body formation rates are rather uncertain and different compilations can be found, for instance, in Abel et al. (2002) and Palla, Salpeter & Stahler (1983).

This paper has been typeset from a TEX/LATEX file prepared by the author.